Acta Metallurgica Sinica (English Letters) (2022) 35:773–789
https://doi.org/10.1007/s40195-021-01342-x

Effect of Annealing Temperature and Strain Rate on Mechanical Property of a Selective Laser Melted 316L Stainless Steel

Hua-Zhen Jiang[1,2] · Zheng-Yang Li[1,2] · Tao Feng[3] · Peng-Yue Wu[3] · Qi-Sheng Chen[1,2] · Shao-Ke Yao[1,2] · Jing-Yu Hou[1,2]

Received: 18 May 2021 / Revised: 12 August 2021 / Accepted: 31 August 2021 / Published online: 5 November 2021

Abstract

In the present work, 316L stainless steel specimens are fabricated by selective laser melting (SLM) via optimized laser process parameters. The effects of two extrinsic factors, i.e., strain rate and annealing temperature, on the mechanical performance of SLM-processed parts are studied. The two intrinsic factors, namely strain rate sensitivity m and work hardening exponent n, which control the tensile properties of the as-built samples, are quantified. Microstructure characterizations show that cellular structure and crystalline grain exhibit apparently different thermal stability at 873 K. Tensile testing reveals that the yield strength decreases from 584 ± 16 MPa to 323 ± 2 MPa, while the elongation to failure increases from $(46 \pm 1)\%$ to $(65 \pm 2)\%$ when annealing temperature varies from 298 K to 1328 K. The n value increases from 0.13 to 0.33 with the increase in annealing temperature. Due to the presence of fine cellular structures and high relative density achieved in as-printed 316L samples, a strong dependence between tensile yield strength and strain rate is observed. In addition, the strain rate sensitivity of the SLM-produced 316L part ($m = 0.017$) is much larger than that of conventional coarse-grained part ($m = 0.006$), whereas the n value increases slightly from 0.097 to 0.14 with increasing strain rate.

Keywords Selective laser melting · 316L stainless steel · Heat treatment · Strain hardening behaviors · Mechanical property

1 Introduction

Laser powder bed fusion, also known as selective laser melting, is one of the additive manufacturing (AM) methods that can produce complex part without part-specific tooling. This technology can result in a microstructure that spans nearly six orders of magnitude in length scales [1], thus distinct mechanical properties that are substantially different from those of manufactured by traditional methods could be attained.

The 316L austenitic stainless steel (316L SS), as an important engineering structural material, has been widely used in the aerospace, nuclear industries, and automotive industries attributed to its admirable physical and mechanical properties (i.e., superior tensile property, excellent weldability, and high corrosion resistance) [2–4]. Thanks to these advantages, an increasing interest has been aroused for researchers who focused on laser metal additive manufacturing of 316L SS [5–9]. In fact, a large number of investigations have been carried out to understand the process parameters-microstructure-property relationships for such an alloy produced by selective laser melting (SLM) [10–14]. Recently, several research groups have reported that high strength and high ductility SLM-processed 316L samples are achievable through manipulating laser process parameters [1, 13, 15–18]. Though different arguments have been reported to address the mechanism for high strength and high ductility attained in SLM-produced 316L sample, these studies do confirm that microstructural features including volume fraction of defects [17, 19], melt pool shape [8, 15], grain size [19], cellular structure size [1, 17], and nanoinclusions [20] have significant effects on the final mechanical property of

Available online at http://link.springer.com/journal/40195.

✉ Zheng-Yang Li
zyli@imech.ac.cn

✉ Qi-Sheng Chen
qschen@imech.ac.cn

[1] School of Engineering Science, University of Chinese Academy of Sciences, Beijing 100190, China

[2] Institute of Mechanics, Chinese Academy of Sciences, Beijing 100190, China

[3] Beijing E-Plus-3D Technology Co., LTD, Beijing 102299, China

the part. To date, most of the studies mainly have focused on the effect of intrinsic microstructures (i.e., grain size [21], nanoinclusions [20], micro-texture [15], defects [13], and residual stresses [22]) on the mechanical properties of the SLM-produced parts. A few studies have investigated the effect of extrinsic factors, for example, strain rate [23, 24] and annealing temperature [25–27], on the mechanical performance of AM-processed parts. A recent work carried out by Ronneberg et al. [26] pointed out that a SLM-manufactured part annealed at a certain temperature can eliminate some unique microstructures (i.e., melt pools, cellular structure, etc.) in the part, and thus the role of a certain microstructure on mechanical property could be revealed. More importantly, SLM-produced 316L samples may experience high impact and dynamic loading during its actual working applications, thus rate dependent deformation behavior should also be unveiled for such an alloy.

In fact, recent studies on the effect of extrinsic factors on mechanical property of SLM-manufactured parts result in contradictory conclusions. For example, Chen et al. [25] reported that SLM-produced 316L samples annealed at 400 °C can lead to a 10% increase in yield strength. The improvement in mechanical property is attributed to the precipitation of nanosized silicate particles [25]. However, such a phenomenon was not observed by other groups [27, 28]. In addition, the effects of strain rate on mechanical property of AM-produced 316L samples were studied by Li et al. [23] and Khodabakhshi et al. [24]. The former concluded that a strong dependence between tensile strength and strain rate was observed whereas the latter reported the opposite. The 316L SS is a face-centered cubic (FCC) material. It is accepted that the flow stress of these conventionally manufactured FCC metals, for example, the 304L SS [29], ultra-fine-grained/nanocrystalline copper [30, 31], and nanocrystalline 316 L SS [32], are strongly strain rate dependent, i.e., the flow stress usually increases as the strain rate is increased. The above contradictory results strongly suggest that a thorough investigation is needed for SLM-produced 316L parts in order to better understand the mechanical response with extrinsic factors.

In this study, the microstructure evolutions at different annealing temperatures are systematically characterized on different planes (i.e., parallel to the build direction and perpendicular to the build direction). The mechanical properties and work hardening ability of the SLM-produced samples at various annealing temperatures are analyzed. In addition, the effect of strain rate on work hardening ability is quantified. The strain rate sensitivity is calculated and compared with the reported values in the literature. Moreover, some clarifications regarding to the contradictory conclusions in literature are also reported in the study based on our experimental results.

2 Experimental

2.1 Sample Preparation and Heat Treatment

Gas-atomized 316L SS powder (Avimetal Powder Metallurgy Technology Co., Ltd, China) with spherical morphology and a particle size ranging from 15 μm to 53 μm was used in this study (Fig. 1a). The chemical composition of the as-used powder is listed in Table 1. Fabrication of the 316L samples were carried out using an EP-M250 machine equipped with a continuous wavelength fiber laser generator with a maximum power of 400 W and typically 80 μm spot diameter. Cuboid-shaped specimens (10 mm (length) × 10 mm (width) × 8 mm (height)) and rectangular bars (45 mm (length) × 10 mm (width) × 10 mm (height)) were fabricated on a 40 mm thick substrate in protection atmosphere of oxygen content below 1000 ppm (Fig. 1e). The optimized laser process parameters used to fabricate 316L samples were laser power 206 W, scanning speed 900 mm/s, hatch spacing 90 μm, and layer thickness 30 μm, respectively [13]. A "zigzag" scanning strategy was used with 67° rotation of the laser scanning direction between successive layers (Fig. 1d). The SLM-produced parts were removed from the baseplate by wire cutting after completion of the building process.

Heat treatments were performed using a chamber furnace with the samples placed into a tube filled with argon gas (Fig. 1b). Samples were subjected to various levels of annealing temperatures with a heating rate between 20 °C/min and 30 °C/min (Fig. 1c). Different heat treatments are used to tailor the microstructure of the parts and are depicted in Table 2. The holding temperatures were 873 K, 1123 K, and 1328 K, respectively (see Table 2).

2.2 Microstructure Characterizations

As-built and heat-treated samples were ground and polished to observe the microstructure on different planes (i.e., top view and side view, Fig. 1e). An acidic water solution containing 2% HF and 8% HNO_3 was used to etch the polished surface. An optical microscope (OM, 55XA) and a scanning electron microscope (SEM, FEI Sirion 400 NC) were used to examine microstructure features of the samples at low and high magnification, respectively. The grain size and misorientation angle distribution of the pars were determined by electron backscattered diffraction (EBSD, EOL JSM-7900F, Japan). All observations were carried out at the position near the middle of the polished surface for a better comparison purpose (Fig. 1e). The specimens were tilted to 70° in the SEM chamber, and an accelerating voltage of 20 kV was used. The scanning

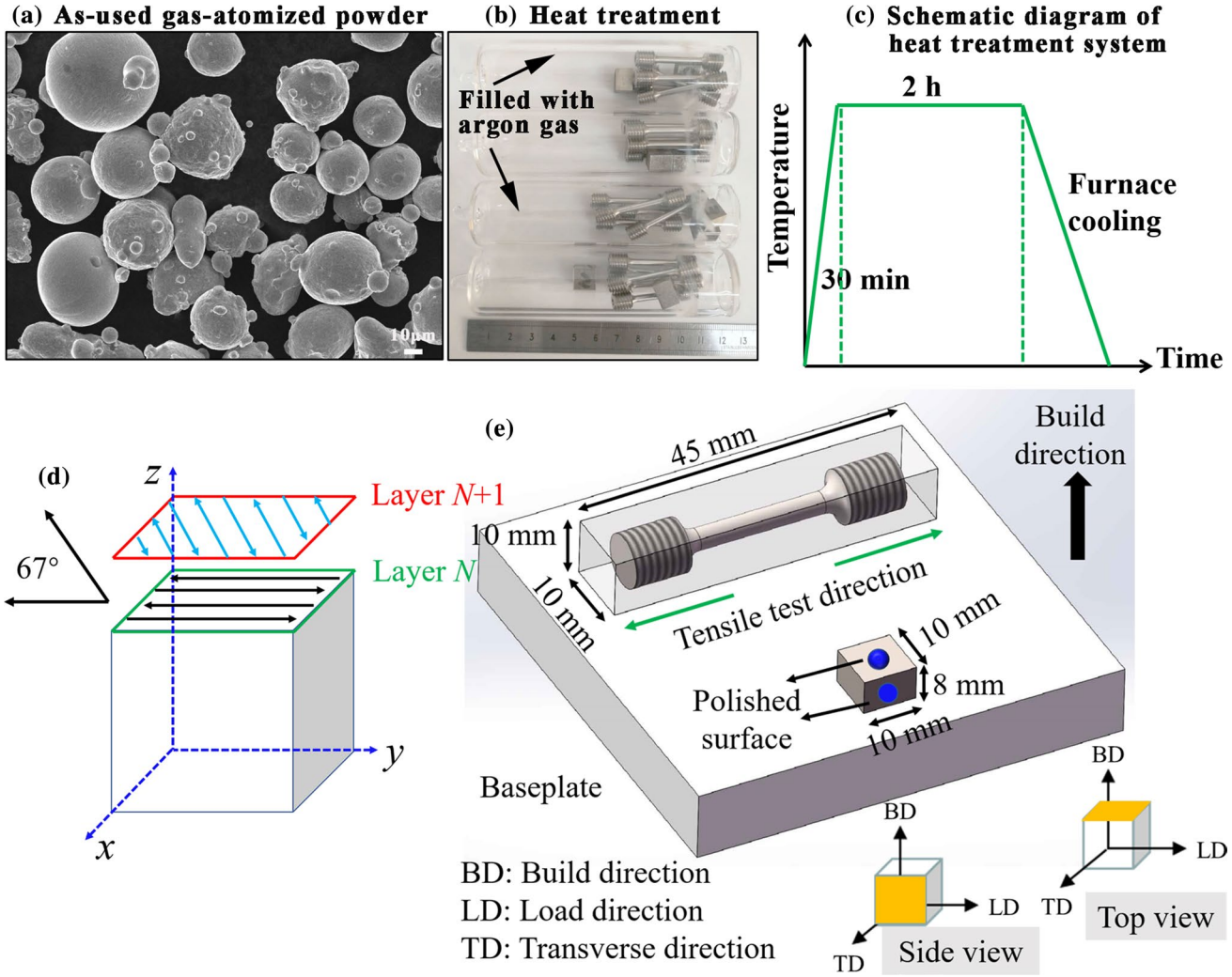

Fig. 1 **a** Morphology of the gas-atomized powders, **b** image of the SLM-produced 316L samples under argon protection, **c** a sketch of the heat treatment process, **d** laser scanning strategy, and **e** sketch of the as-fabricated specimens which the tensile specimen extraction scheme and the position selected for microstructure observation are clearly shown

Table 1 Chemical composition of as-used 316L SS powder (wt.%)

Fe	Cr	Ni	Mo	Mn	Si	C	P	S
Bal	18.84	10.68	2.26	1.05	0.91	≤0.03	≤0.04	≤0.01

Table 2 Heat treatments applied to the 316L SS samples

Samples	Heat treatment conditions
As-built	–
(Heat treatment 1) HT1	873 K + 2 h, furnace cooling
(Heat treatment 2) HT2	1123 K + 2 h, furnace cooling
(Heat treatment 3) HT3	1328 K + 2 h, furnace cooling

step was set as 1 μm during the experiment. Data analysis was performed with the TSL-OIM analysis software. After tensile test, the fracture morphologies of the SLM-produced specimens were observed by SEM.

2.3 Hardness and Tensile Tests

Vickers microhardness (HV) tests with a 1 kg load and 15 s dwelling time were conducted on metallographic parts using the "Everone MH-6" microhardness tester. A total of seven

microhardness measurements were taken for each SLM-processed sample.

The as-built rectangular bars were machined to standard dogbone samples with a diameter of 3 mm and gauge length of 15 mm according to ISO 6892–1: 2009. Uniaxial tensile tests were performed at room temperature on an Electronic Universal Testing Machine (CMT5105S, China) at the strain rate of 2.2×10^{-3} s^{-1} for as-built and annealed samples. The reported mechanical properties were the average results of five tests with the same process parameters. Different strain rate tests (i.e., 5.6×10^{-5} s^{-1}, 2.2×10^{-3} s^{-1}, 2.2×10^{-2} s^{-1}, and 2.2×10^{-1} s^{-1}) were conducted to calculate the m value and n value of as-built sample. The n values of the as-built parts subjected to different annealing temperatures were also obtained by tensile tests at a strain rate of 2.2×10^{-3} s^{-1}.

3 Results and Discussion

3.1 Effect of Annealing Temperature on Microstructure of a SLM-Processed Part

3.1.1 Melt Pool and Cell Structure Evolution

Previous study reported that the as-built part presents hierarchical structures in macro, micro, and nanoscales [2]. These length scales include melt pools, columnar grains, low-angle grain boundaries (LAGBs), cellular network structures, and oxide nanoinclusions, respectively [1, 2, 23]. Figure 2a–f shows the macroscale structures for SLM-manufactured parts subjected to different annealing temperatures on top surface and side surface. The microstructure including melt pool morphology and cellular structure of the as-built part was presented elsewhere [13] and hence was not provided in this study. It is observed that the melt pool traces on both planes (side plane and top plane) are still visible when samples are treated at 873 K (Fig. 2e and f). The high magnified SEM images reveal the presence of cellular structures with cell sizes ranging between 0.4 μm and 0.5 μm (Fig. 3). The melt pool morphology and cell structure size are basically consistent with that of the as-built part [13]. This result suggests that heat treatment temperature below 873 K does not significantly change the microstructure of the SLM-produced part. The role of heat treatment at temperature around 873 K is mainly to reduce the microscale residual stress of the part [33].

After annealing at 1123 K, the melt pool traces and cellular structures are almost dissolved while irregular grains are observed (Fig. 2c and d and Fig. 3). The grains on the two planes show an apparently different morphology: the crystalline grains on top surface include small and large equiaxed grains, and some elongated grains are also observed (Fig. 2c), whereas the grains on side plane are almost elongated strips in shape and grow along the build direction (Fig. 2d). SEM observations reveal that a large number of white particles were mainly located at the grain boundaries on the two observed planes in the sample (Fig. 3). Comparison of concentration of these white particles with the matrix can be depicted from energy-dispersive X-ray spectroscopy (EDS) analysis results shown in Fig. 4. It can be found that these particles contain mostly Si, Mo, and Cr. Previous studies reported that Si has a higher chemical affinity with oxygen at high temperature than the rest of the elements in the 316L SS and tends to preferentially react with the residual oxygen in the chamber [20, 34]. The observed white particles are therefore most likely to be particles containing Si, Mo, and Cr. The precipitated particles have been widely reported in as-built 316L SS [2] and its annealed samples [25, 28], which is in accord with the results shown in this study. Note that the deformation resistance of a SLM-produced part can be improved due to these white particle precipitates along grain boundaries at this annealing temperature (i.e., precipitation strengthening). Although the substructure of the part at annealing temperature of 1123 K is nearly dissolved compared with the as-built sample, the reduction of the tensile property and microhardness is little (see Sect. 3.2 in the following), suggesting that the precipitated white particles play an important role in mechanical response of the part.

At 1328 K, no melt pools and substructures can be observed. The grain size of the material is obviously coarsened compared with that of other heat-treated samples. There is no apparent difference in grain morphology on the two observed planes (Fig. 2a and b, Fig. 3). In addition, only a few white particles can be observed compared with that of samples annealed at 1123 K. The precipitates are believed to become larger while their number decreases when annealing temperature increases [28]. The change in white particle content was reported to be associated with dissolution of the particles [25], and our result indicates that these white particles are gradually dissolved at elevated temperature over than 1123 K.

3.1.2 Grain Size and LAGBs Evolution

Although the changes in microstructure of the material under different annealing temperatures can be observed from the OM and SEM images, quantitatively analysis of the grain size evolution of the samples in these images is difficult. Figure 5a–d depicts the grain maps of the as-built and annealed parts. The microstructure of the as-built 316L sample is a checkerboard-like structure on the top surface but is a columnar grain structure on the side plane (Fig. 5a). The columnar grains grow along the build direction and cross several melt pools of different layers, showing an obvious epitaxial grain growth characteristic. The microstructure

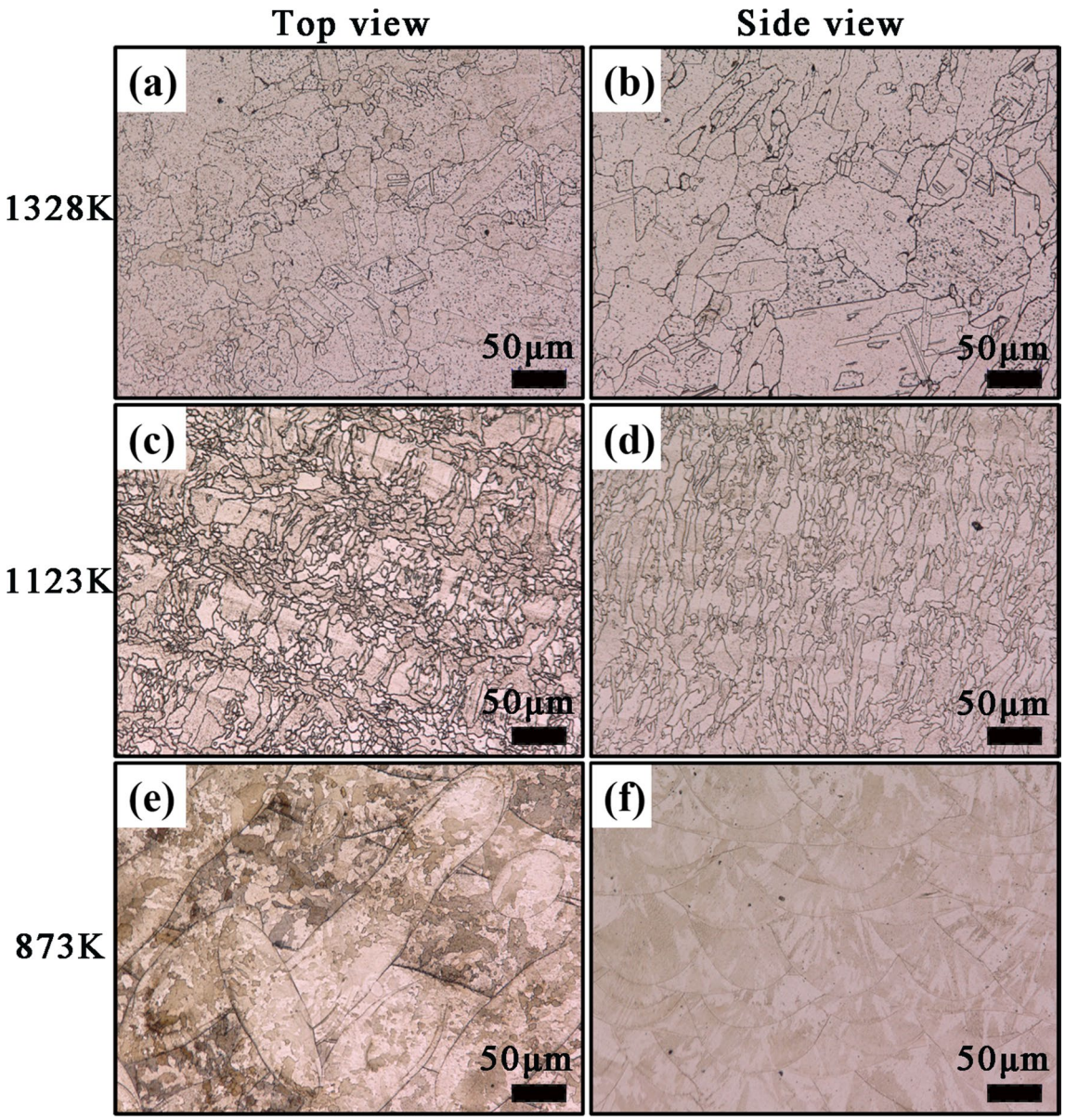

Fig. 2 Optical microstructures of heat-treated samples at temperatures of 1328 K, 1123 K, and 873 K, respectively. **a**, **c**, **e** Top view; **b**, **d**, **f** side view

appearance is typical in SLM-produced material because SLM is decorated with rapid melting and solidification far from equilibrium conditions [17]. Such a microstructure feature has also been widely reported in the literature [11, 25, 35] which is consistent with the observation in this study. The corresponding grain size distributions on the top surface in the images are presented in Fig. 5e–h. It can be observed that the grains in all of the heat-treated samples are roughly equiaxed from the top view, however, the grains are elongated and the direction of elongated grain is paralleling to build direction when annealing temperature is below 1123 K from the side view (Fig. 5a–c). As annealing temperature reaches 1328 K, there are no evident differences between the two planes in terms of grain morphology and grain size (Fig. 5d and Fig. 6a). The result suggests that anisotropic yield behavior might be weak when SLM-produced parts are heat-treated at temperature above 1328 K.

At 873 K, there are many small grains (< 10 μm) agglomerate around the large grains (Fig. 5a). As annealing temperature increases to 1123 K, the percentage of small grains slightly decreases while the maximum grain size shows an apparently increasing trend (the grain size can be as high as 76.6 μm, see Fig. 5g). The large number of white particles precipitated along grain boundaries can act as nucleation

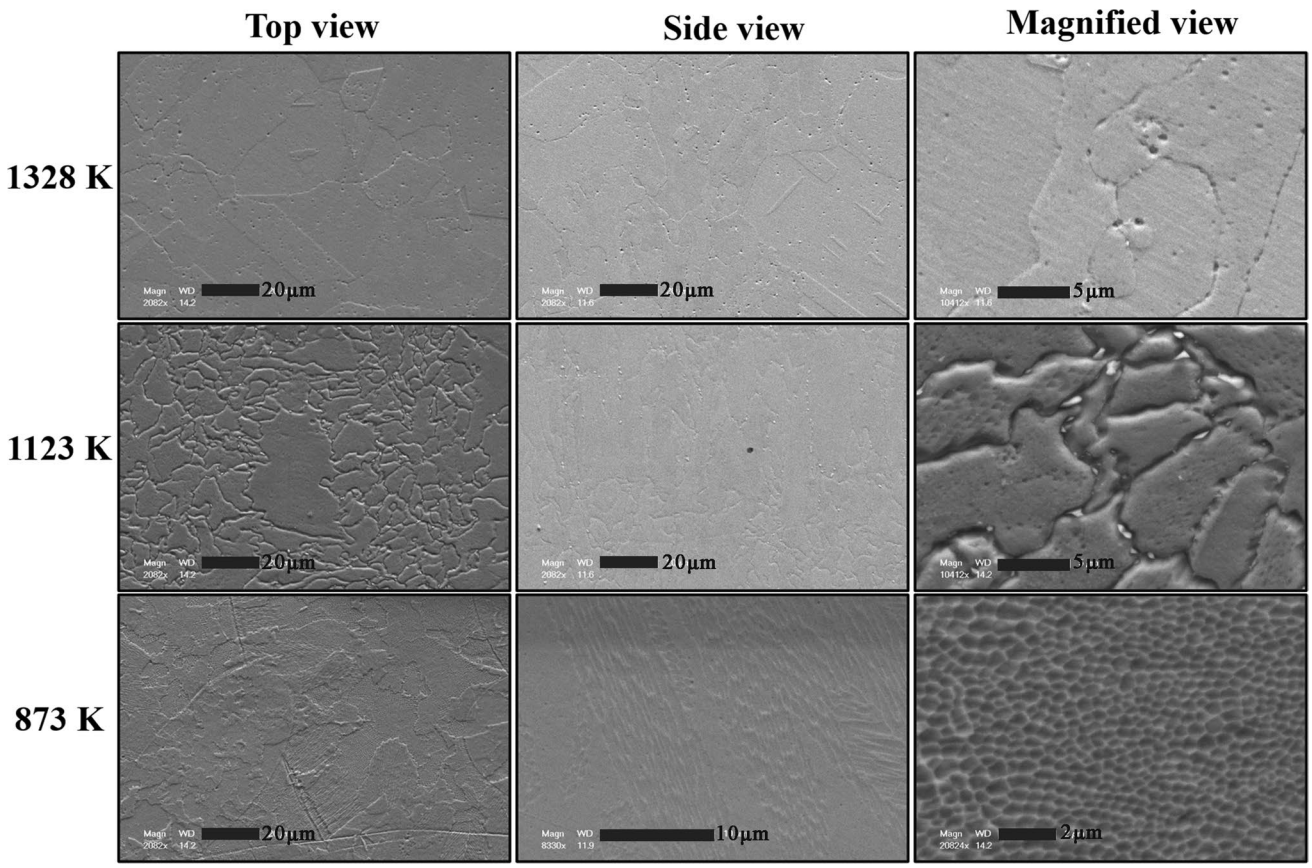

Fig. 3 SEM images of SLM-processed samples heat-treated at various temperatures

sites during heat treatment (Fig. 3), whereas the holding temperature and holding time are not sufficient high enough to make those newly formed small grains grow large enough, hence grain size decreases as compared with that of as-built part. The percentage of small grains show a sharp decreasing trend whereas the maximum grain size continues to increase when annealing temperature is 1328 K, leading to an average grain size up to 36.56 ± 21.12 μm (Fig. 5d, h, and Fig. 6a). To better understand the effect of annealing temperature on grain size of SLM-produced parts, we compared our experimental results with previous studies. From the results listed in Table 3, it is observed that the effect of annealing temperature on grain size is quite divergent in the literature. A closer look at the heat-treated conditions, it is found that both the annealing temperature and holding time play an important role in grain size evolution. Overall, the grain size remains nearly unchanged if both low annealing temperature ($\leq$650 °C) and holding time ($\leq$2 h) is used [15, 28, 36]. The grain size will show an apparently increasing trend if holding time is significantly increased [27]. However, grain size refinement of the as-built parts may also occur under some certain heat-treated conditions [25, 37]. The average grain size for as-built sample is larger than those of annealed samples (see Fig. 6a). If the classical Hall–Petch relation is used to predict the yield strength of SLM-manufactured part, a higher grain size should result in lower yield strength. However, the mechanical properties of the SLM-produced parts annealed at 873 K are basically the same as that of the as-built state sample (see Fig. 8c–d), which otherwise suggests that the mechanical property of a SLM-processed part is mainly controlled by its subgrain structures instead of grain size determined by HAGBs [1].

The band contrast maps for SLM-manufactured parts annealed at different temperatures are displayed in Fig. 7. In this study, low-angle grain boundaries (LAGBs) are defined as 2°-10°, whereas misorientation angle exceeds 10° is considered as high-angle grain boundaries (HAGBs) [1]. It shows that the fraction of LAGBs shows a decreasing trend as the annealing temperature increases (from 76%–78% in the as-printed sample to 11%–26% in sample annealed at 1328 K, see Fig. 6b and Fig. 7e–h). This means that the LAGBs are unstable during heat treatment process. Compared with the as-built samples, it is observed that the cellular structure size remains stable, while the grain size/morphology and the fraction of LAGBs start to change at 873 K, suggesting that these

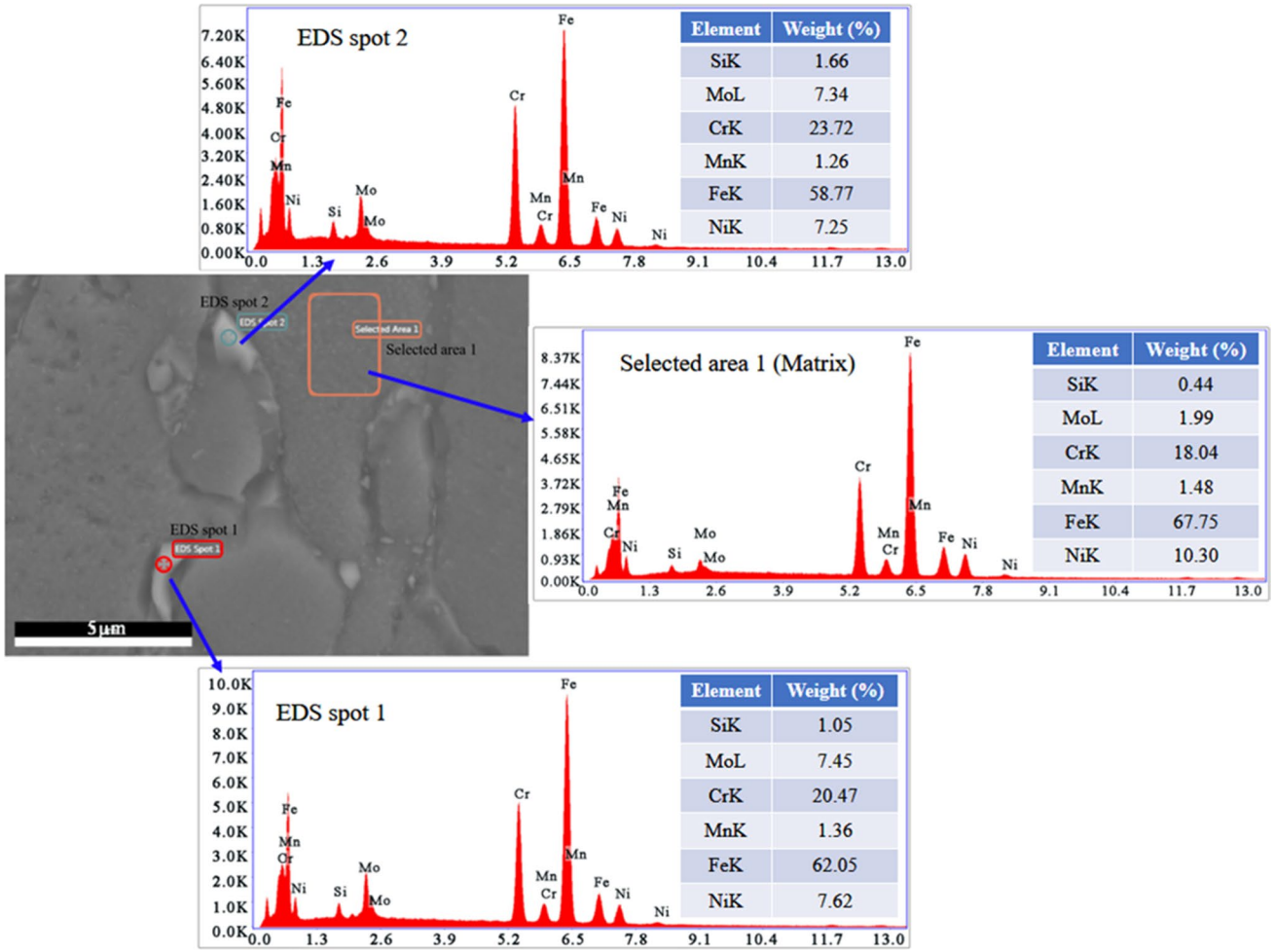

Fig. 4 EDS analysis result of the white particles

structures have apparently different thermal stability at annealing temperature of 873 K (see Figs. 2, 3, 5, and 6). In addition, we notice that SLM-produced parts annealed at 1328 K can lead to a significant increasement of Σ3 twin boundaries (Σ3, at 60°, the percentage is 26%–47% of the total boundaries, Fig. 7h), suggesting the formation of annealing twins [16]. The result indicates that a partial recrystallization occurs at annealing temperature of 1328 K. The formation of annealing twins can enhance the work hardening ability of the SLM-processed part during plastic deformation (see next section, Fig. 9), hence the onset of plastic instability is delayed [16]. On the one hand, the twin boundaries can act as obstacles to dislocation movement [16]. On the other hand, gliding of dislocations along twin boundaries is feasible due to the presence of coherent Σ3 structure [38]. As a result, a better ductility is achieved for samples annealed at 1328 K (see Fig. 8a–c).

3.2 Effect of Annealing Temperature on Mechanical Property and Work Hardening Behavior of a SLM-Produced Sample

The representative tensile engineering and true stress–strain curves of the SLM-produced parts at different annealing temperatures are displayed in Fig. 8a and Fig. 8b, respectively. The corresponding tensile properties of the parts are shown in Fig. 8c. It shows that yield strength (YS), ultimate tensile strength (UTS), and elongation to failure (ε_f) remain nearly unchanged for samples annealed at a temperature up to 873 K. When annealing temperature is over than 873 K, the YS value decreases continuously while the ε_f value increases, resulting in the so-called strength-ductility trade off behavior. Note that the reduction in YS value is small (from 584 MPa at as-built state to 513 MPa) when annealing temperature increases to 1123 K, whereas it shows an apparently decreasing trend (from 584 MPa to 323 MPa)

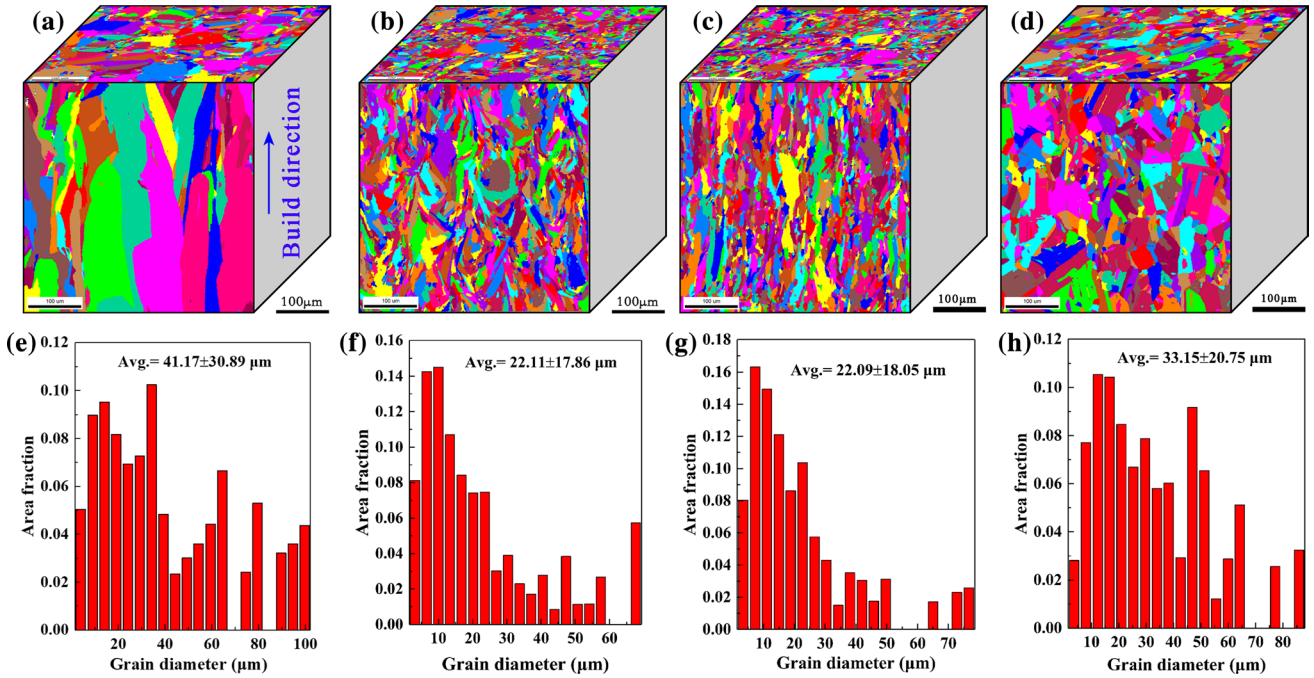

Fig. 5 Grains maps of as-built and annealed 316L SS samples. The grain maps on the side surfaces are similar to each other; hence only one map paralleling to build direction is presented in these figures. The grain size distribution is obtained from the top surface in the image. **a** As-built, **b** 873 K, **c** 1123 K, **d** 1328 K. **e**, **f**, **g**, **h** Corresponding grain size distributions for as-built, 873 K, 1123 K, and 1328 K sample, respectively

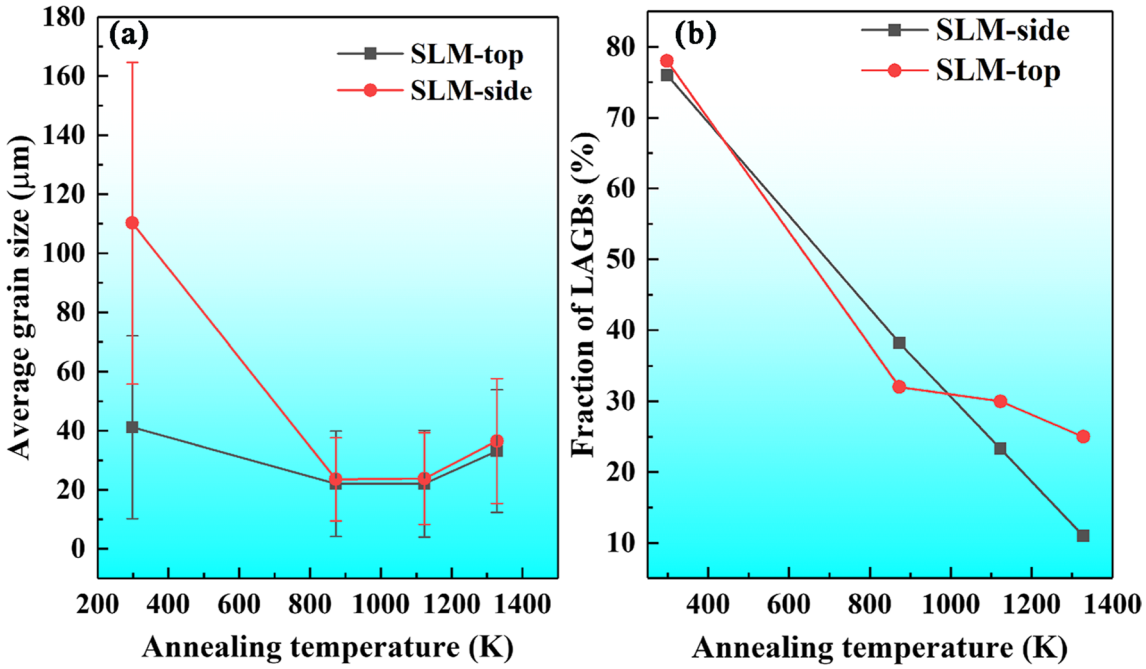

Fig. 6 Summary of average grain size and fraction of LAGBs as a function of annealing temperature. **a** Average grain size, **b** fraction of LAGBs

when samples are treated at 1328 K. To better understand the mechanical response versus annealing temperature, we compared our results to those reported in the literature (Fig. 8e). Though different YS values for as-produced 316L samples were reported by many other research groups (450 MPa to 650 MPa), the YS value shows a similar evolution trend with

Table 3 Summary of grain size changes as a function of the annealing temperature

References	Conditions	Grain size
[a]Montero-Sistiaga et al. [36]	The as-built samples are heat-treated under argon atmosphere at 600 °C and 950 °C for 2 h, followed by air cooling, whereas the 1095 °C annealed samples are water cooled	The grain length is ~ 100 µm. There is no difference in grain size in comparison with the as-built samples
[a]Ding et al. [37]	The as-produced samples are annealed for 3 h at 400 °C and 900 °C, followed by furnace cooling	The difference in grain size between 400 °C annealed sample and as-built sample is little, whereas the grain size is refined after annealing at 900 °C
[b]O.O. Salman et al. [27]	The as-built samples are heat-treated under argon atmosphere at 573 K, 873 K, 1273 K, 1373 K, and 1673 K for 6 h	The average grain size increases from 45 µm, 50 µm, 55 µm, 65 µm, 88 µm to 102 µm as annealing temperature increases from 573 K to 1673 K
[c]Chen et al. [25]	The as-produced samples are annealed for 1 h at 400 °C and 800 °C, followed by water cooling	The average grain size slightly decreases from 5.9 µm to 5.4 µm as annealing temperature increases
[b]Voisin et al. [28]	The as-built samples are annealed every 200 °C from 400 °C to 1200 °C for 1 h	The average grain size remains nearly the same up to 800 °C. Overall, the grain size shows an increasing trend (from ~ 9 µm to ~ 18 µm) when annealing temperature is raised from room temperature to 1200 °C
[a]Sun et al. [15]	The as-built samples are annealed at 650 °C in vacuum condition for 2 h, followed by furnace cooling	There is little sign of grain growth for SLM-produced samples

[a]The grain size is calculated from side plane.
[b]The grain size is calculated from top plane.
[c]Denotes that the grain size is calculated by an area reconstruction method from both top plane and side plane.

annealing temperature. Overall, the tensile yield strength of a SLM-produced sample remains nearly unchanged for samples annealed up to 873 K, which is in accord with the stability of cellular structures observed in this study (Fig. 3). However, compared with the variation of its corresponding YS values with annealing temperature, the change in UTS value is little (see Fig. 8f). The microhardness results on top surface and side surface of the parts are presented in Fig. 8d. There is only a little difference between the two observed planes for microhardness at various annealing temperatures. The microhardness of the as-built sample is ~ 256 HV_1, which is typical of hardness achieved by SLM (Fig. 8g). Note that the hardness of as-printed sample is rather diverse. This is mainly because the adopted laser process parameters are different in the literature, resulting in different microstructures and porosity contents in the sample [5, 39]. Also, it shows a similar trend to that of yield strength as a function of annealing temperature when annealing temperature is over than 1123 K (decrease from 258 HV_1 at as-built state to 199 HV_1 at 1328 K). Despite of the large variation of hardness values reported in the literature at a certain annealing temperature, it shows a decreasing trend with the increase of annealing temperature (Fig. 8g).

To understand the work hardening behaviors of the as-built parts and the annealed samples, the normalized work hardening rate curves (normalized by a shear modulus of 74 GPa for 316L SS [15]) as a function of true strain are presented in Fig. 9a. The normalized work hardening rate is calculated as $\theta = (d\sigma/d\varepsilon)/G$, where σ, ε, and G are the true stress, true strain, and shear modulus, respectively. It is observed that the work hardening behaviors of the as-built samples and the annealed samples are all characterized with three distinct stages. Stage I: The θ value decreases sharply at the initial stage of material deformation; Stage II: The reduction in θ value slows down and keeps this stage for a wide range; Stage III: The θ value decreases again rapidly due to plastic instability of the material occurs. Though the hierarchical microstructure of the SLM-produced sample is nearly unchanged after annealing at 873 K, the work hardening rate in 873 K sample is relatively larger than that of as-built sample before the onset of necking happens. The similar result is also observed by Chen et al. [22] who reported that samples annealed at 500 °C leads to an increased strain hardening rate in annealed samples than as-printed samples. The behavior could be attributed to the relaxation of printing-induced non-equilibrium microstructures and associated microscale residual stresses in as-built samples [22, 33]. However, compared with work hardening rate curves of the samples annealed at a higher temperature (i.e., 1123 K and 1328 K), the 873 K sample shows a relatively little difference with as-built sample. This is because cellular structures remain stable at 873 K (Fig. 3). Previous studies have shown that these cellular walls are decorated with a high density of dislocations [1, 17, 28], hence the dislocation nucleation rate is lower

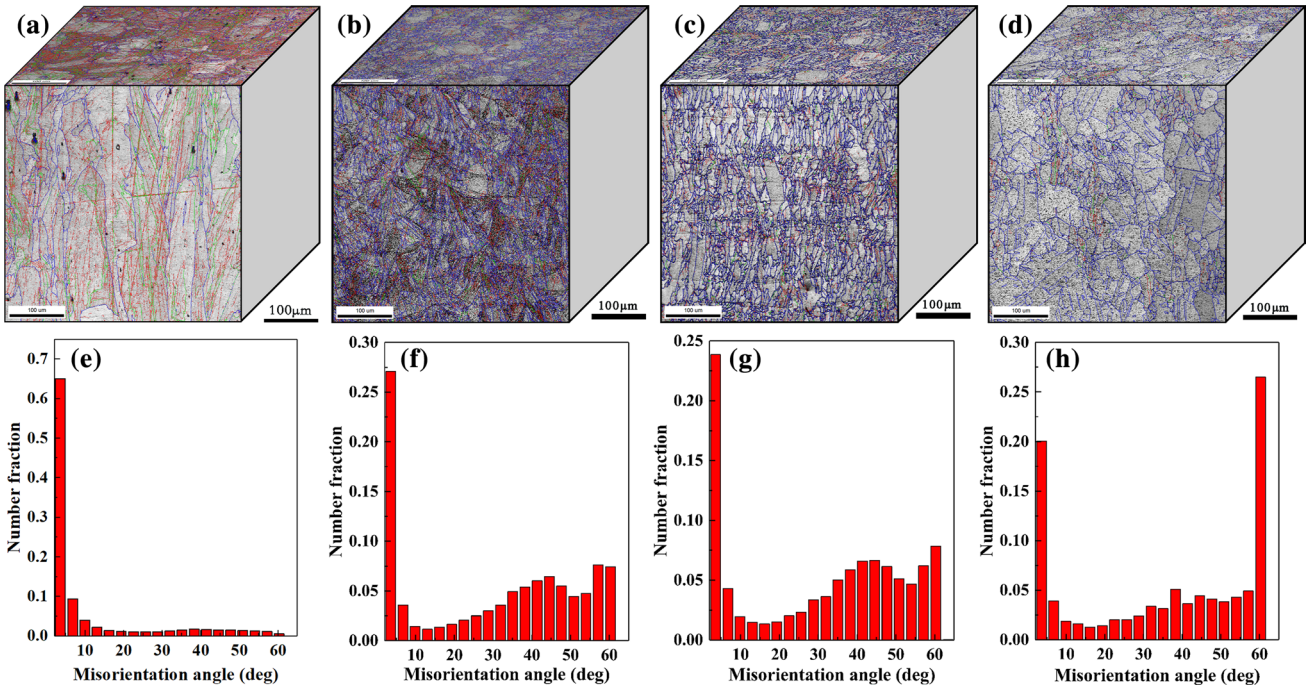

Fig. 7 Band contrast maps of as-built and annealed 316L SS samples. The misorientation angle distribution is obtained from the top surface in the image. A misorientation angle between 2° and 5° is colored in red, 5°–15° is colored in green, whereas 15°–180° is colored in blue. **a** As-built, **b** 873 K, **c** 1123 K, **d** 1328 K. **e**, **f**, **g h** Corresponding misorientation angle distributions for as-built, 873 K, 1123 K, and 1328 K sample, respectively

due to the loose dislocations will initially move in the microstructure before nucleation becomes energetically favorable at higher stress levels [28]. However, the work hardening ability of the material is significantly improved after the annealing temperature exceeds 1123 K. This is evidenced by a higher work hardening rate in the early stage of deformation and a longer period of work hardening (Fig. 9a). Compared with the annealed samples, the work hardening rate of the as-built part is relatively poor (Fig. 9a). Nevertheless, considering the normalized work hardening regimes fall within 0.01–0.03, which is consistent with the reported values for the high strength and high ductility SLM-processed 316L parts [15, 16]. Compared the mechanical property of 1328 K annealed sample with the reported wrought 316L SS, it is observed that SLM-produced samples annealed at 1328 K have a combination of both excellent yield strength and good ductility which is comparable or better than its corresponding wrought counterpart (see Fig. 8h).

In general, increasing the ductility of a part can be achieved by delaying the onset of necking. According to Hart [48], plastic instability takes place when the following criterion is satisfied:

$$d\sigma/d\varepsilon + m \cdot \sigma \leq \sigma. \tag{1}$$

The work hardening exponent can be obtained by the following Ludwik–Hollomon equation:

$$n = \frac{\partial \ln \sigma}{\partial \ln \varepsilon}, \tag{2}$$

Therefore, the n value can be obtained by logarithmic plots of σ versus ε when strain rate is constant.

The strain rate sensitivity can be calculated as

$$m = \left(\frac{\partial \ln \sigma}{\partial \ln \dot{\varepsilon}}\right), \tag{3}$$

where $\dot{\varepsilon}$ is the strain rate. Hence, the m value can be determined by logarithmic plots of σ versus $\dot{\varepsilon}$. From the above equations, it is evident that both the strain hardening ($d\sigma/d\varepsilon$) and strain rate hardening ($m{\cdot}\sigma$) play an important role in the delay of necking. The work hardening exponent n and strain rate sensitivity m of the SLM-produced part are quantified in the study.

Figure 9b shows the logarithmic plots of true stress versus true strain for the SLM-manufactured parts at various annealing temperatures. It is observed that the n value increases from 0.13 to 0.33 as the annealing temperature increases from 298 K (room temperature) to 1328 K. The n value at 1328 K is almost three times larger than that of the as-built part. Also, the n value for the 873 K

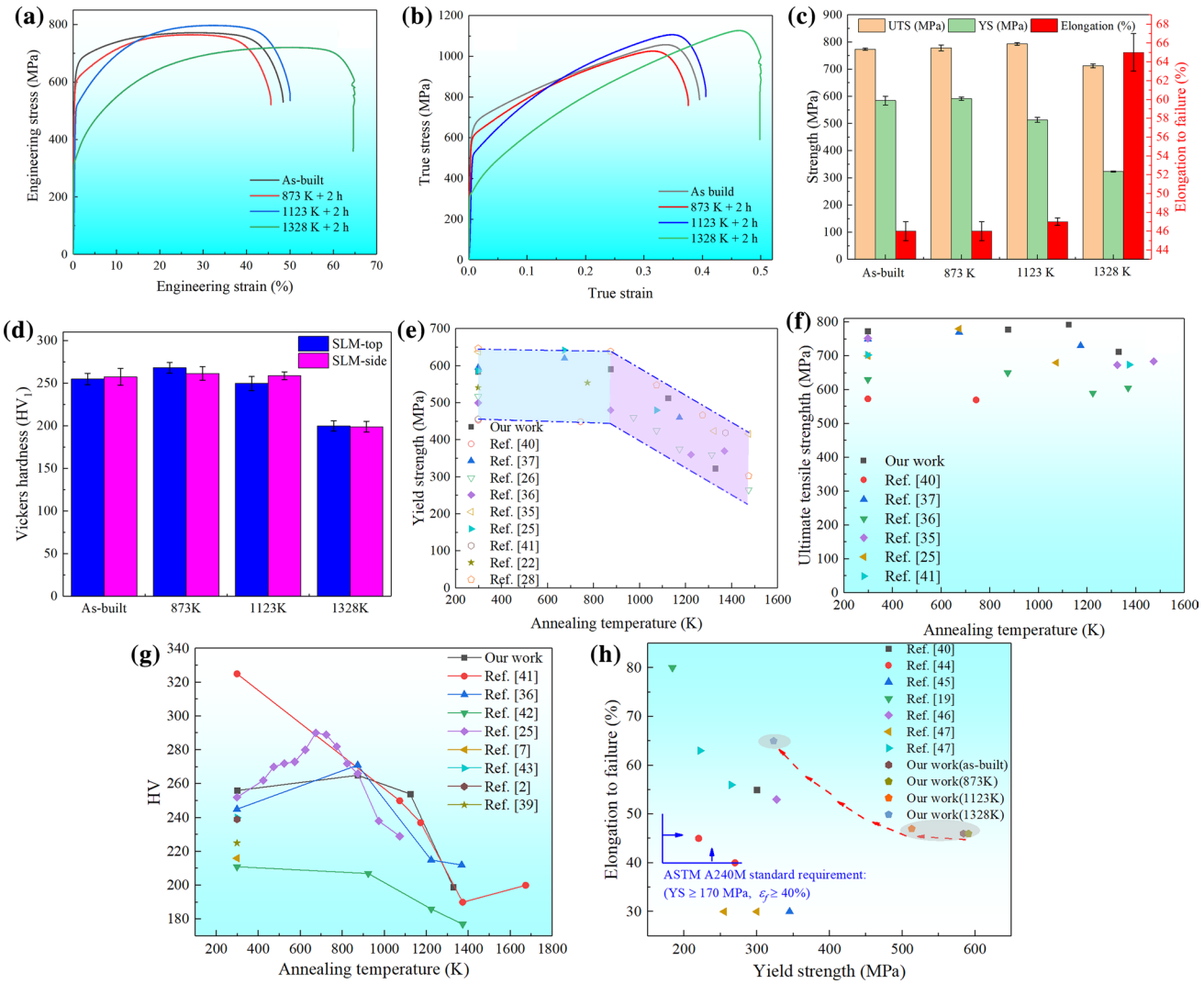

Fig. 8 Effect of annealing temperature on the mechanical property of SLM-processed parts. **a** and **b** Representative engineering tensile stress–strain curves and the corresponding true stress-true strain curves at various annealing temperatures. **c** and **d** Summary of tensile properties and microhardness of SLM-produced parts as a function of annealing temperature, respectively. **e** Variation of yield strength with annealing temperature including our work and data reported in the literature. The blue dashed lines indicate the general variation trend. **f** Ultimate tensile strength as a function of annealing temperature based on reported values in the literature. **g** Hardness as a function of annealing temperature for our work and researches reported in the literature. **h** Comparison between the obtained mechanical properties in this study and wrought 316L (including cold finished and solution treated) reported in the literature. The red dashed lines indicate the general trend of mechanical response for samples annealed at different temperatures. The above data are collected from references [2, 7, 19, 22, 25, 26, 28, 35–37, 39–47]

annealed sample is 0.16, which is very close to that of the as-built sample (the value is 0.13). The result suggests that although the work hardening behavior is altered for SLM-produced samples heat-treated at 873 K (see Fig. 9a), the work hardening ability of the SLM-produced 316L SS is nearly unchanged, which otherwise indicates that the presence of cellular structure at 873 K sample is of great importance to mechanical performance of the part. It should be emphasized that the calculated *n* values for samples annealed at different temperatures are determined by considering the entire plastic deformation process. As shown in Fig. 9b, the slope of the tangent line, which indicates the *n* value of the sample, increases with true strain at the initial stage of deformation, but it will be stabilized as the deformation continues. Hence, the calculated *n* value can be regarded as an average value for the annealed sample during the entire plastic deformation. This result also indicates that a shift of deformation mechanism occurs during the plastic deformation. According to the in situ synchrotron X-ray diffraction experiments carried out by Wang et al. [1], dislocation slip is the dominant deformation mechanism when the applied strain is relatively low (i.e., 3%), whereas twinning becomes an important mechanism as the deformation continues. The

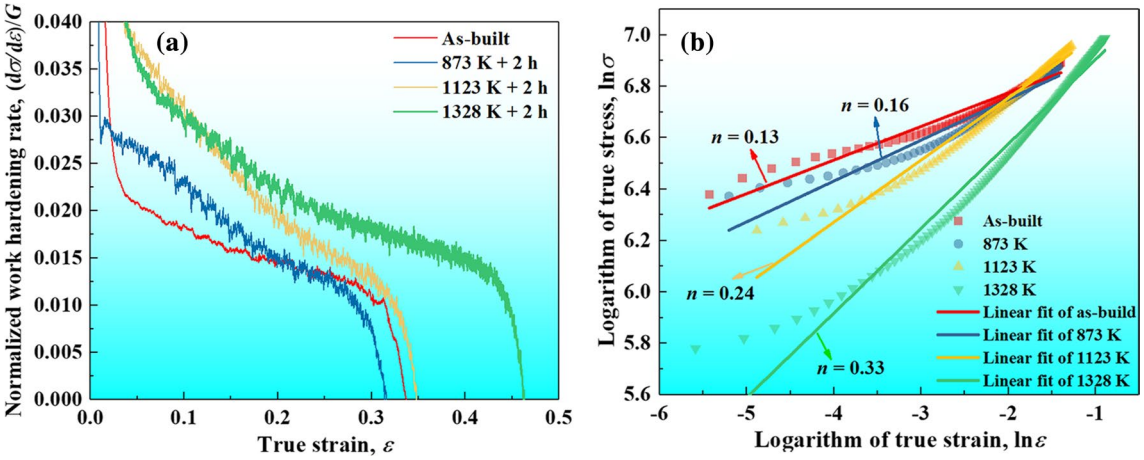

Fig. 9 Effect of annealing temperatures on strain hardening behavior of SLM-produced parts. **a** Normalized work hardening rate curves as a function of annealing temperature, **b** logarithmic plots of true stress versus true strain for the SLMed parts at various annealing temperatures

intersections for twin–twin and twin–cellular walls can provide a unique three dimensional network for progressive and steady work hardening in SLM-produced 316L sample [1]. Hence, the *n* value remains stable after the deformation twinning is dominated at a high strain level (see Fig. 9b).

The fracture surface morphologies of the annealed samples after tensile test are shown in Fig. 10. Compared with the fracture morphology of as-built sample [13], samples annealed at different temperatures still appear ductile fracture with many submicron sized dimples (Fig. 10b, d, and f), suggesting that all of the samples (as-built and annealed parts) have good plasticity. The SLM-produced part annealed at 873 K still has a certain proportion of small pores (Fig. 10e, f), whereas the pores tend to disappear as annealing temperature increases (Fig. 10a–d). In addition, it is observed that both the density and depth of the dimples increase as annealing temperature increases especially at 1328 K (Fig. 10b). Such dense and deep ductile dimples can increase the area of fracture surface and absorb more deformation energy during the tensile deformation process. Hence, the ductility is improved as annealing temperature increases. The observations are consistent with the results of the tensile test (Fig. 8a).

3.3 Effect of Strain Rate on Mechanical Property, Work Hardening Exponent, and Strain Rate Sensitivity of a SLM-Produced Part

Tensile tests are conducted at several strain rates to elucidate the rate-controlling deformation mechanism of a SLM-produced part. The representative engineering stress–strain curves of SLM-produced parts at different strain rates are shown in Fig. 11a. The YS value and UTS value increase monotonously from (614 ± 6) MPa and (753 ± 4) MPa to (702 ± 4) MPa and (794 ± 3) MPa, respectively, while the elongation to failure drops from (49 ± 2)% to (34 ± 2)% when strain rate increases from 5.6×10^{-5} s^{-1} s to 2.2×10^{-1} s^{-1}. The yield strength and ultimate tensile strength of SLM-produced 316L samples increase with increasing strain rate, yielding a significant rate-strengthening effect (Fig. 11a, b). The result is consistent with the study of Li et al. [23] but contradicts the result of Khodabakhshi et al. [24]. In the study of Khodabakhshi et al. [24], the 316L samples were prepared by laser metal deposition (LMD). They concluded that the strain rate had no obvious effect on LMD-manufactured 316L SS samples. The above contradictory results may stem from the following two reasons: (1) the cooling rate in the melt pool for SLM-produced sample is about two orders of magnitude larger than that of LMD-deposited sample [49], resulting in a distinct microstructure difference for samples manufactured by the above two fabrication methods. We compared the microstructure features between the works carried out by Khodabakhshi et al. [24] and ours. The cell size in the study of Khodabakhshi et al. [24] is about 10 μm–15 μm, which is much larger than the cell size of the SLM-produced sample in this study (the cell size is ~ 0.43 μm). Also, an aspect ratio of ~ 40 was reported in the study of Khodabakhshi et al. [24], where the grain width and grain length are ~13.4 μm and 500 μm, respectively. The aspect ratio of grain size is much higher than that of this study (~ 2.7). Therefore, the relatively larger grain size and substructure size might be responsible for a lack of strain-rate dependency for the LMD-produced samples; (2) As shown in Fig. 11a, b, the elongation to failure decreases with increased strain rate (from 49% to 34%). In fact, the built-in flaws have a great effect on elongation to failure for SLM-processed parts under uniaxial tensile test [13, 23]. Hence, it can be concluded that the internal defects in additive manufactured parts are very sensitive to strain rate. The 316L

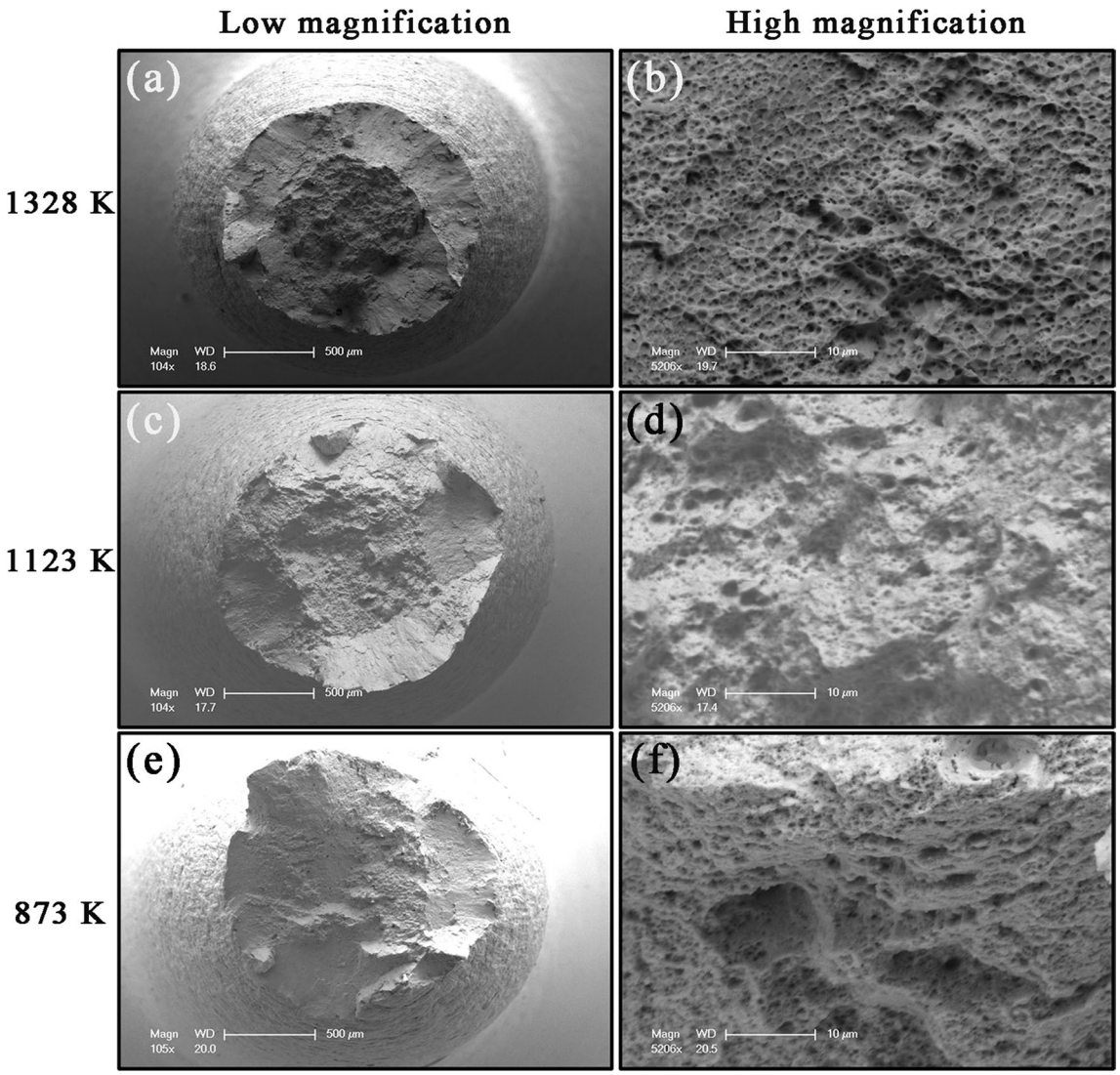

Fig. 10 Fracture surfaces of SLMed 316L SS at different annealing temperatures

sample fabricated by LMD has pores with a length scale over than 200 μm, and a long crack with a characteristic length up to ~ 1 mm is also observed based on the macro-OM images provided by Khodabakhshi et al. [24]. However, the relative density of SLM-processed sample in this study is measured to be (99.8 ± 0.03)% (Fig. 12). It is observed that most of the defects are spherical in shape and randomly located in the sample. The maximum defect size is ~ 30.12 μm in arbitrary four regions. The formation of these defects is likely due to the entrapment of the shielding gas [39] or transfer of as-used powder pore sources to the part [50]. Tensile test at a high strain rate promotes the SLM-processed part to fail prematurely, resulting in an underestimated value for elongation to failure. Therefore, the process-induced larger pores and cracks may also be one of the possible reasons for LMD-processed sample lack of strain-rate dependency.

The work hardening exponent and strain rate sensitivity of SLM-produced 316L parts are calculated according to Eqs. (2 and 3), and the results are shown in Fig. 11c, d. It can be observed that the n value decreases slightly from 0.14 to 0.097 as the strain rate increases from 5.6×10^{-5} s^{-1} to 2.2×10^{-1} s^{-1}, suggesting that the effect of strain rate on the work hardening ability of a SLM-manufactured part is weak. We further calculated the m value of the SLM-manufactured part according to Eq. (3), and the result is 0.017 (Fig. 11d). The estimated m value in this study is three to four times larger than the coarse-grained 316L sample (the m value is 0.0061 [24]) and is comparable to those of nanostructured metals (the m value of nanocrystalline copper and nanocrystalline nickel is ~ 0.03) [31]. In addition, the calculated m value in this study is not much different from that of Li et al.

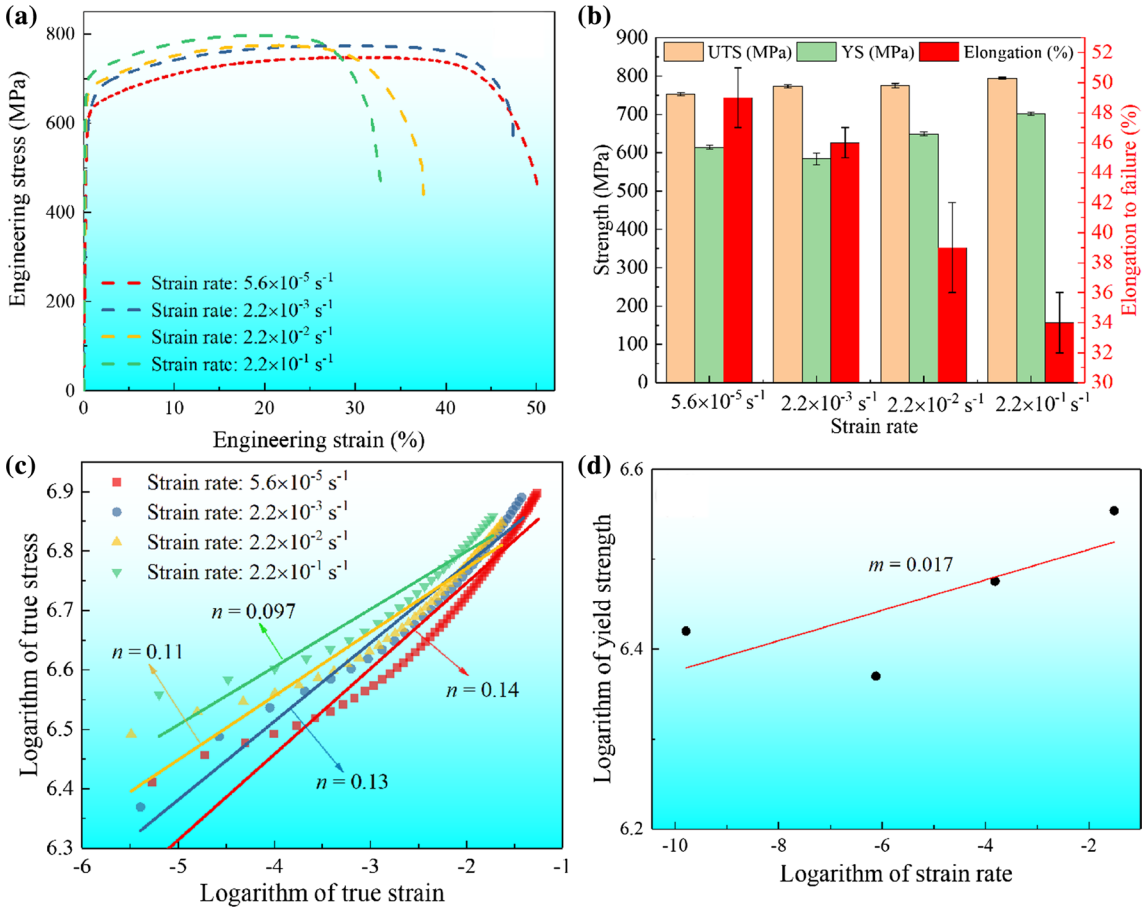

Fig. 11 **a** Representative engineering tensile stress–strain curves at different strain rates. **b** Summary of tensile properties of SLM-produced part at different strain rates. **c** Logarithmic plots of true stress versus true strain for the SLMed material at different strain rates. **d** Logarithmic plots of tensile strength versus strain rate for the SLMed material

who reported that the m value for SLM-produced high strength and high ductility 316L sample is 0.022 [23]. This higher m value is the intrinsic reason for SLM-produced 316L SS sample with high ductility.

Figure 13 displays the fractographic features of SLM-produced parts at different strain rates. At macro-level, one can observe that all samples show a "cup-shaped" feature with a certain necking, indicating a typical ductile fracture characteristic. In addition, a few small pores are also observed in all of the tested samples (Fig. 13a, c, e, g). At micro-level, it is observed that at the same magnification, the fractured surfaces of the samples tested at different strain rates are still occupied by a large number of submicron sized dimples. However, the depth and density of the dimples decrease with the increased strain rate, indicating that the ductility of the SLM-produced sample decreases with the increase of strain rate. This is completely in agreement with the tensile test result shown in Fig. 11a, b.

4 Conclusions

In summary, the effects of annealing temperature and strain rate on the resultant mechanical properties of SLM-processed parts are investigated in this research. The two intrinsic factors which control the tensile properties of as-built part, namely work hardening exponent n and strain rate sensitivity m, are quantified. The main conclusions can be drawn as follows:

(1) The cellular structure and crystalline grain show apparently different thermal stability during the heat treatment process. SLM-produced samples annealed at 873 K lead to a decrease in grain size whereas the cell structure size remains stable. The cellular structures and a large fraction of LAGBs contribute to the high strength and high ductility of the as-built parts compared with the annealed specimens.

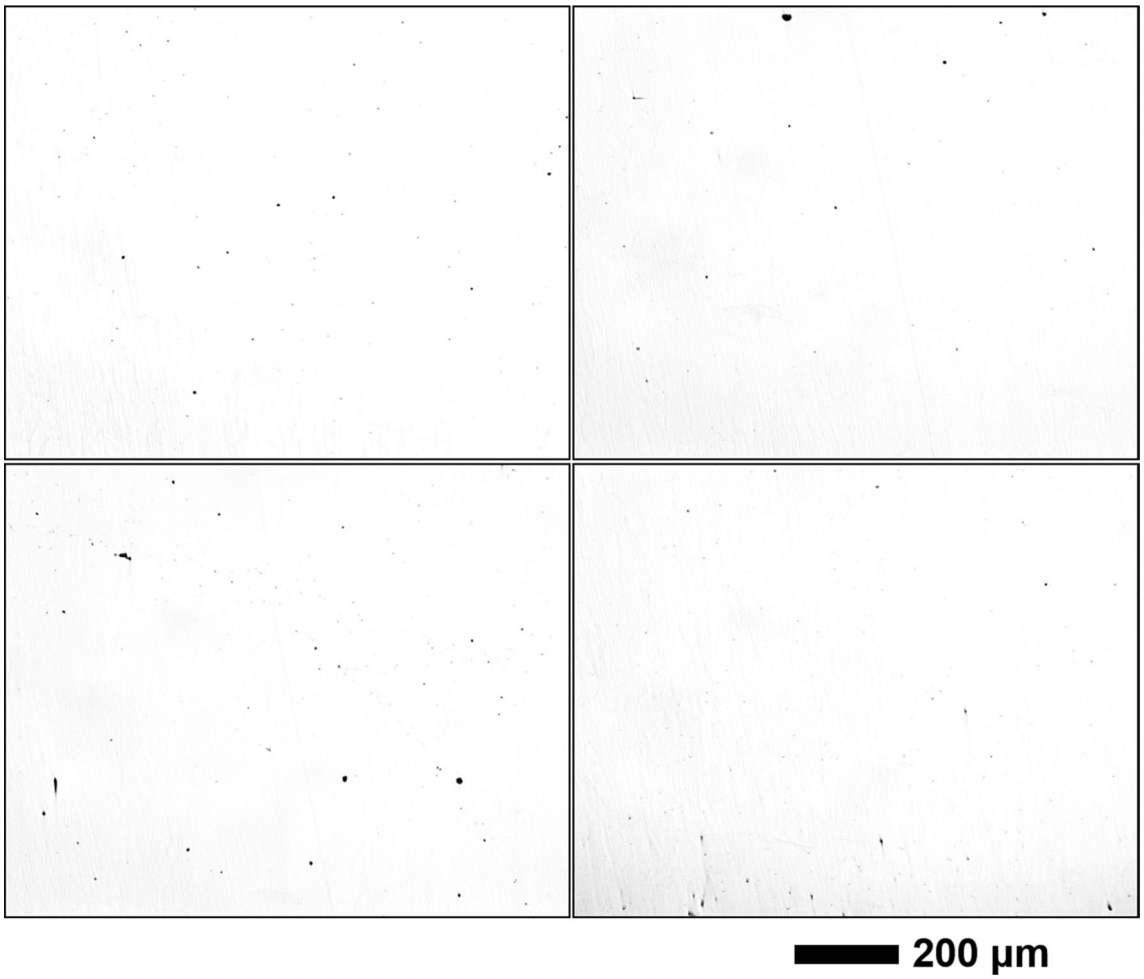

Fig. 12 Optical micrographs of polished sections showing porosity in as-built sample

(2) The SLM-produced parts annealed at 873 K lead to a mechanical performance as that of the as-built part whereas heat treatment at temperature over than 1123 K results in the classical strength-ductility trade-off behavior. The presence of fine cellular structures and fewer built-in flaws in as-printed 316L SS sample are responsible for the strong dependence between tensile strength and strain rate.

(3) The work hardening exponent increases from 0.13 to 0.33 when annealing temperature increases from 298 K to 1328 K. However, the effect of strain rate on n value is not noticeable (from 0.14 to 0.097 as strain rate increases). A relatively higher strain rate sensitivity ($m \sim 0.017$) is observed for SLM-produced part compared to that of coarse-grained counterparts ($m \sim 0.0061$).

(4) Ductile fracture is the main failure mode for samples annealed at different temperatures and tensile tested at different strain rates. The fracture surfaces are always decorated with a large number of submicron sized dimples, which helps to increase fracture surface area and absorb more deformation energy during tensile test, thus improving the ductility of the sample.

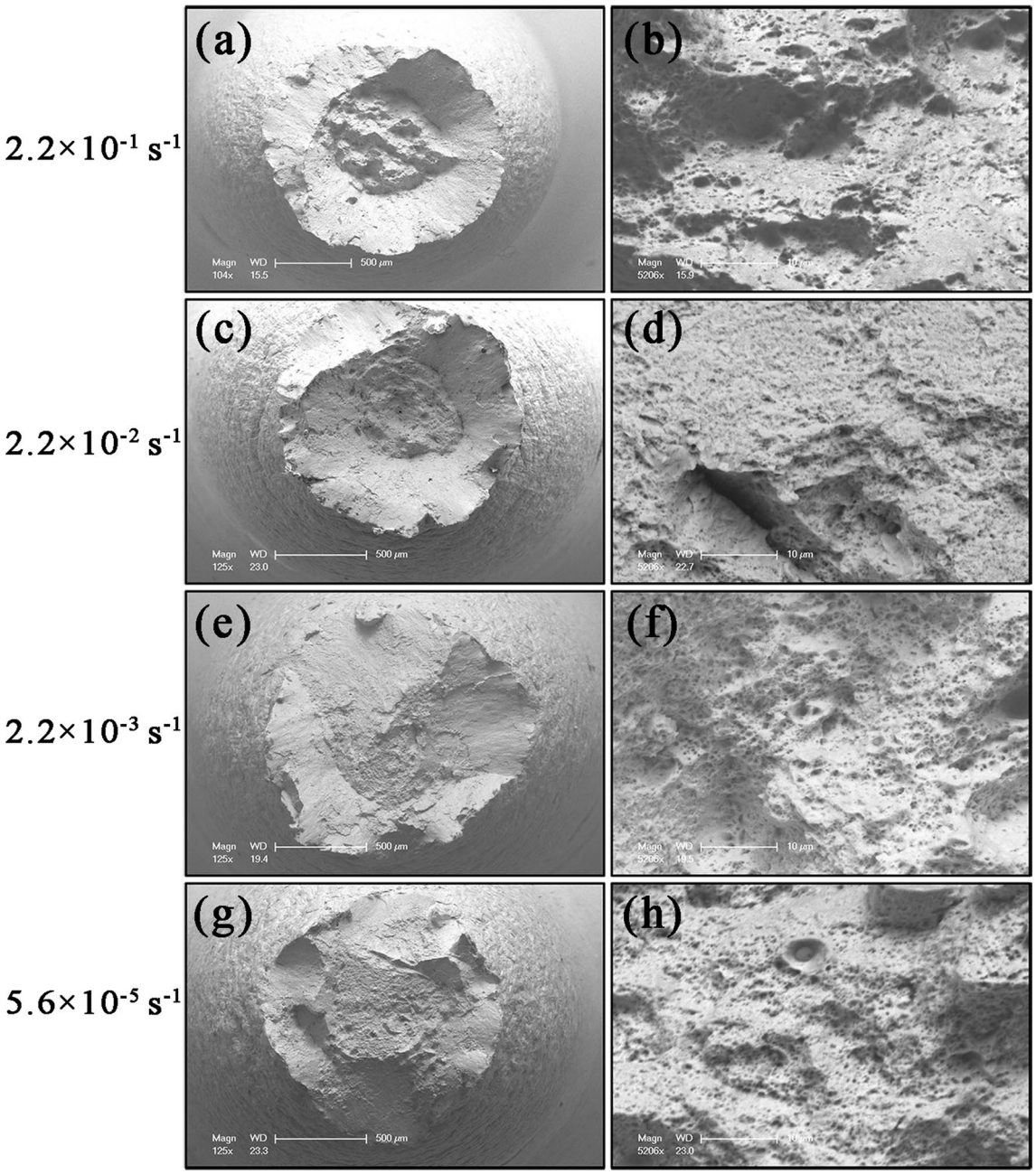

Fig. 13 Fracture surfaces of SLM-produced parts at different strain rates

Acknowledgements This work was supported by the National Natural Science Foundation of China (Grant No. 11772344) and National Key R&D Program of China (Project No. 2016YFB1100700). The authors acknowledge engineers Yun-Long Feng and Long-Fei Chen for their experimental assistance of sample manufacturing process.

Declarations

Conflict of interest The authors state that there are no conflicts of interest to disclose.

References

[1] Y.M. Wang, T. Voisin, J.T. McKeown, J. Ye, N.P. Calta, Z. Li, Z. Zeng, Y. Zhang, W. Chen, T.T. Roehling, R.T. Ott, M.K. Santala, P.J. Depond, M.J. Matthews, A.V. Hamza, T. Zhu, Nat. Mater. **17**, 63 (2018)

[2] Y. Zhong, L.F. Liu, S. Wikman, D.Q. Cui, Z.J. Shen, J. Nucl. Mater. **470**, 170 (2016)

[3] M. Kazemipour, M. Mohammadi, E. Mfoumou, A.M. Nasiri, JOM **71**, 3230 (2019)

[4] M. Ziętala, T. Durejko, M. Polański, I. Kunce, T. Płociński, W. Zieliński, M. Łazińska, W. Stępniowski, T. Czujko, K.J. Kurzydłowski, Z. Bojar, Mater. Sci. Eng. A **677**, 1 (2016)
[5] H.Z. Jiang, Z.Y. Li, T. Feng, P.Y. Wu, Q.S. Chen, Y.L. Feng, S.W. Li, H. Gao, H.J. Xu, Opt. Laser. Technol. **119**, 105592 (2019)
[6] J. Suryawanshi, K.G. Prashanth, U. Ramamurty, Mater. Sci. Eng. A **696**, 113 (2017)
[7] Z.J. Sun, X.P. Tan, S.B. Tor, W.Y. Yeong, Mater. Des. **104**, 197 (2016)
[8] S.-H. Sun, T. Ishimoto, K. Hagihara, Y. Tsutsumi, T. Hanawa, T. Nakano, Scripta Mater. **159**, 89 (2019)
[9] K. Lin, D. Gu, L. Xi, L. Yuan, S. Niu, P. Lv, Q. Ge, Int. J. Adv. Manuf. Technol. **104**, 2669 (2019)
[10] D. Wang, C.H. Song, Y.Q. Yang, Y.C. Bai, Mater. Des. **100**, 291 (2016)
[11] M.L. Montero-Sistiaga, M. Godino-Martinez, K. Boschmans, J.P. Kruth, J. Van Humbeeck, K. Vanmeensel, Addit. Manuf. **23**, 402 (2018)
[12] T. Kurzynowski, K. Gruber, W. Stopyra, B. Kuźnicka, E. Chlebus, Mater. Sci. Eng. A **718**, 64 (2018)
[13] H.Z. Jiang, Z.Y. Li, T. Feng, P.Y. Wu, Q.S. Chen, Y.L. Feng, L.F. Chen, J.Y. Hou, H.J. Xu, Acta Metall. Sin. -Engl. Lett. **34**, 495 (2020)
[14] R. Casati, J. Lemke, M. Vedani, J. Mater. Sci. Technol. **32**, 738 (2016)
[15] Z.J. Sun, X.P. Tan, S.B. Tor, C.K. Chua, NPG. Asia. Mater. **10**, 127 (2018)
[16] M. Shamsujjoha, S.R. Agnew, J.M. Fitz-Gerald, W.R. Moore, T.A. Newman, Metall. Mater. Trans. A **49**, 3011 (2018)
[17] L. Liu, Q. Ding, Y. Zhong, J. Zou, J. Wu, Y.-L. Chiu, J. Li, Z. Zhang, Q. Yu, Z. Shen, Mater. Today. **21**, 354 (2018)
[18] Y. Yin, J. Sun, J. Guo, X. Kan, D. Yang, Mater. Sci. Eng. A **744**, 773 (2019)
[19] S. Bahl, S. Mishra, K. Yazar, I.R. Kola, K. Chatterjee, S. Suwas, Addit. Manuf. **28**, 65 (2019)
[20] K. Saeidi, L. Kvetkova, F. Lofajc, Z.J. Shen, RSC Adv. **5**, 20747 (2015)
[21] M. Ma, Z. Wang, X. Zeng, Mater. Sci. Eng. A **685**, 265 (2017)
[22] W. Chen, T. Voisin, Y. Zhang, J.-B. Florien, C.M. Spadaccini, D.L. McDowell, T. Zhu, Y.M. Wang, Nat. Commun. **10**, 1 (2019)
[23] Z. Li, T. Voisin, J.T. McKeown, J.C. Ye, T. Braun, C. Kamath, W.E. King, Y.M. Wang, Int. J. Plasticity. **120**, 395 (2019)
[24] F. Khodabakhshi, M. Farshidianfar, A. Gerlich, M. Nosko, V. Trembošová, A. Khajepour, Mater. Sci. Eng. A **756**, 545 (2019)
[25] N. Chen, G. Ma, W. Zhu, A. Godfrey, Z. Shen, G. Wu, X. Huang, Mater. Sci. Eng. A **759**, 65 (2019)
[26] T. Ronneberg, C.M. Davies, P.A. Hooper, Mater. Des. **189**, 108481 (2020)
[27] O. Salman, C. Gammer, A. Chaubey, J. Eckert, S. Scudino, Mater. Sci. Eng. A **748**, 205 (2019)
[28] T. Voisin, J.-B. Forien, A. Perron, S. Aubry, N. Bertin, A. Samanta, A. Baker, Y.M. Wang, Acta Mater. **203**, 116476 (2021)
[29] M. Stout, P. Follansbee, J. Eng. Mater.-T. ASME **108**, 344 (1986)
[30] A. Mishra, M. Martin, N.N. Thadhani, B.K. Kad, E.A. Kenik, M.A. Meyers, Acta Mater. **56**, 2770 (2008)
[31] Y. Wang, E. Ma, Mater. Sci. Eng. A **375**, 46 (2004)
[32] A. Husain, P. La, Y. Hongzheng, S. Jie, Materials **13**, 3223 (2020)
[33] D. Kong, X. Ni, C. Dong, L. Zhang, C. Man, J. Yao, K. Xiao, X. Li, Electrochim. Acta **276**, 293 (2018)
[34] W.M. Tucho, V.H. Lysne, H. Austbø, A. Sjolyst-Kverneland, V. Hansen, J. Alloys Compd. **740**, 910 (2018)
[35] D. Kong, C. Dong, X. Ni, L. Zhang, J. Yao, C. Man, X. Cheng, K. Xiao, X. Li, J. Mater. Sci. Technol. **35**, 1499 (2019)
[36] M. Montero Sistiaga, S. Nardone, C. Hautfenne, J. Van Humbeeck, Effect of heat treatment of 316L stainless steel produced by selective laser melting (SLM). in *Proceedings of the 27th Annual International Solid Freeform Fabrication Symposium-An Additive Manufacturing Conference*, The University of Texas, Austin, Texas, 8–10 July 2016
[37] L. Ding, H.X. Li, Y.D. Wang, Z.T. Huang, Chin. J. Las. **42**, 187 (2015)
[38] K. Lu, L. Lu, S. Suresh, Science **324**, 349 (2009)
[39] J.A. Cherry, H.M. Davies, S. Mehmood, N.P. Lavery, S.G.R. Brown, J. Sienz, Int. J. Adv. Manuf. Technol. **76**, 869 (2015)
[40] C. Elangeswaran, A. Cutolo, G.K. Muralidharan, C. de Formanoir, F. Berto, K. Vanmeensel, B. Van Hooreweder, Int. J. Fatigue **123**, 31 (2019)
[41] K. Saeidi, X. Gao, F. Lofaj, L. Kvetková, Z.J. Shen, J. Alloys Compd. **633**, 463 (2015)
[42] M. Kamariah, W. Harun, N. Khalil, F. Ahmad, M. Ismail, S. Sharif, Effect of heat treatment on mechanical properties and microstructure of selective laser melting 316L stainless steel. in *4th International Conference on Mechanical Engineering Research, Swiss Garden Beach Resort*, Malaysia, 1–2 August 2017
[43] J.P. Choi, G.H. Shin, M. Brochu, Y.J. Kim, S.S. Yang, K.T. Kim, D.Y. Yang, C.W. Lee, J.H. Yu, Mater. Trans. **57**, 1952 (2016)
[44] I. Tolosa, F. Garciandía, F. Zubiri, F. Zapirain, A. Esnaola, Int. J. Adv. Manuf. Technol. **51**, 639 (2010)
[45] T.M. Mower, M.J. Long, Mater. Sci. Eng. A **651**, 198 (2016)
[46] I.A. Segura, L.E. Murr, C.A. Terrazas, D. Bermudez, J. Mireles, V.S.V. Injeti, K. Li, B. Yu, R.D.K. Misra, R.B. Wicker, J. Mater. Sci. Technol. **35**, 351 (2019)
[47] X. Chen, J. Li, X. Cheng, B. He, H. Wang, Z. Huang, Mater. Sci. Eng. A **703**, 567 (2017)
[48] E.W. Hart, Acta Metall. **15**, 351 (1967)
[49] D. Herzog, V. Seyda, E. Wycisk, C. Emmelmann, Acta Mater. **117**, 371 (2016)
[50] R. Cunningham, S.P. Narra, C. Montgomery, J. Beuth, A.D. Rollett, JOM **69**, 479 (2017)